Available online at www.sciencedirect.com

Manufacturing Letters

Manufacturing Letters 00 (2023) 000–000

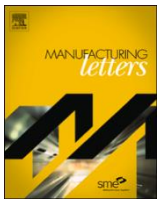

51st SME North American Manufacturing Research Conference (NAMRC 51, 2023)

Copper-Nickel Functionally Magnetic Gradient Material Fabricated via Directed Energy Deposition

Manikanta Grandhi[a], Vy Nguyen[a], Zhichao Liu [a,*], Cesar-Octavio Romo-De-La-cruz[b] and Xueyan Song[b]

[a]*Department of Industrial and Management Systems Engineering, West Virginia University, Morgantown, WV 26506, USA*
[b]*Department of Mechanical and Aerospace Engineering, West Virginia University, Morgantown, WV 26506, USA*

* Corresponding author. Tel.: +1-806-620-0566. *E-mail address:* zhichao.liu@mail.wvu.edu

Abstract

In this paper, a functional gradient material (FGM) of CuSn10 and Inconel 718 is fabricated through a laser-based directed energy deposition (DED) additive manufacturing process. Experimental studies are performed to examine the microstructures, the interface bonding behaviors, and the physical and mechanical properties of the resulting FGMs. The result shows that a sound metallurgical bonding was formed at the interface section. The electrical resistivity for CuSn10, IN718, and CuSn10 – IN718 samples are tested for a temperature range of 320 to 390K, CuSn10 – IN718 specimen displayed its value in the middle range of its counterparts. The CuSn10 – IN718 FGM displayed the highest absolute Seebeck coefficient in the temperature range 320K to 390K. The change in the Seebeck coefficient of the FGM showed a 70% increase from the single material specimens. This boost indicated a reduction in carrier density across the interface, theorized to be influenced by the interface of the FGM. During the compression strength test, a folding deformation occurred in the copper alloy region but neither buckling nor deformation was triggered at the interface section.

*Keywords:*Directed Energy Deposition (DED); Functionally Gradient Material (FGM); Microstructure;Conductivity

1. Introduction

Additive manufacturing (AM) can produce structures with complex designs and tailored material properties. With a layer-upon-layer fabrication route, it facilitates the creation of divergent metal composites by directly bonding one to another, therefore, promoting continuous changes in material properties across. Directed energy deposition (DED) is one of the laser-based AM processes in which three-dimensional parts can be directly fabricated from raw materials with a layer additive method. Due to flexible and controllable composition feed, laser-based DED is more adaptable and expedient to produce various gradient materials from thick coatings to complex bulk structures with better bond strength and mechanical properties [1]. Functionally gradient material (FGM) is innovative material in which final properties vary gradually with dimensions. It possesses varying compositions and thus, varying material and mechanical properties. When designing FGMs via AM, the selection of metal composites is centered on an application with perplex mechanical, physical-metallurgical properties, especially with large variations in thermal expansion coefficient or detrimental compound formation between dissimilar components of a part [2-3].

A commercially available nickel-based superalloy–Inconel 718 (IN718) is a magnetic material that has been extensively used in aerospace applications because of its outstanding high-temperature strength, creep, toughness,

and corrosion resistance [4]. However, its low thermal conductivity constrains its usage in heat exchange and thermal energy conversion applications [5]. Similarly, a copper-based alloy – CuSn10 is a non-magnetic softer and ductile metal with high thermal and electrical conductivity known for its high resistance against salt and alkaline corrosion [6]. Thus CuSn10 – IN718 FGMs aid in compensating for the low thermal properties of IN718, and such bimetallic structures have demand in industries such as space, aviation, and marine [7].

Copper-and-nickel-based FGMs are expected to possess both materials' advantages, including but not limited to thermal and electrical conductivity, high-temperature withholding, high strength and toughness, and corrosion resistance, and can be utilized in many industries and applications. Though proven Ni-based alloys are metallurgically compatible with Cu through different AM processes [8-9], during Laser-AM printing higher reflectivity and thermal conductivity properties of Cu alloy cause fractious faulty builds due to unstable laser plasma heat flux [10]. Substantially, the interactive and bonding behaviors between CuSn10 and IN718 were not clearly understood with the laser-DED approach. Therefore, it is desirable to examine the microstructures, and properties, including both mechanical and physical, of the resulting CuSn10 and IN718 gradient specimens, as well as the feasibility of manufacturing such specimens via the DED AM mechanism. The research studies [11-12] utilized AM techniques to fabricate nickel – copper bimetallic structures to understand the effect of the copper mass fraction on the thermo-mechanical properties of the graded parts. They concluded that metal composite variations would alter mechanical properties like porosity, tensile strength, yield strength, and hardness.

In this paper, an FGM part is fabricated with IN718 and CuSn10 through a hybrid directed energy deposition (DED) system to achieve the following two goals: (1) Determining the feasibility of fabricating CuSn10 and IN718 FGMs via DED AM, and (2) Investigating the physical and mechanical properties and the microstructures of the resulting FGMs. The physical property tests comprised electrical conductivity and Seebeck coefficient measurements. The microstructure analysis and mechanical testing include microscopic imaging, scanning electron microscopy (SEM), energy dispersive spectroscopy (EDS), and hardness test. In addition, a compressive strength test is performed to analyze the interface bonding behaviors.

2. Materials and Methods

2.1. Materials

A gas-atomized CuSn10 powder with a particle size of 45-105 μm supplied from MSE Supplies LLC is used. CuSn10 is a strengthened copper alloy with 10 % tin. Similarly, IN718 powder (Carpenter Additive, USA) is used with a particle size range of 45-106 μm. Fig. 1 and Fig. 2 depicts the SEM images for CuSn10 and IN718 powders. The respective powder chemical compositions are presented in Table 1 and Table 2.

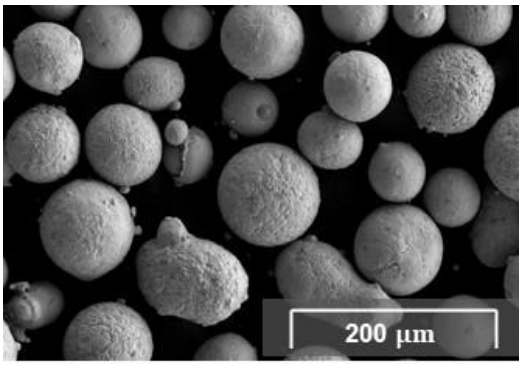

Fig. 1. SEM micrograph of CuSn10 powder

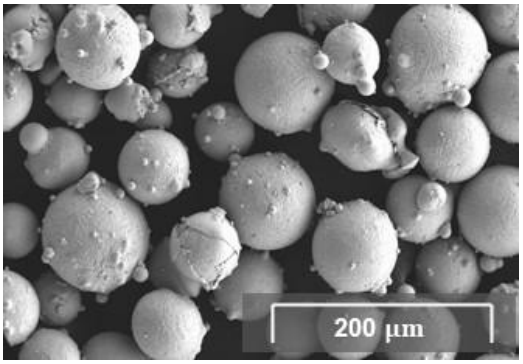

Fig. 2. SEM micrograph of IN718 powder

Table 1. Chemical composition of CuSn10 (% weight)

Element	Sn	Zn	Pb	P	Ni	Al
%	9.2~11.5	0.05	0.25	0.60~1.0	0.1	0.01
Element	Fe	Mn	Cu			
%	0.08	0.05	Bal.			

Table 2. Chemical composition of IN718 (% weight)

Element	Al	Cr	Fe	Mo	Ni	Nb
%	0.7	20.5	18.5	2.9	51.6	4.8
Element	Ti	Cu	others			
%	0.8	0.15	Bal.			

2.2. Directed energy deposition (DED) of CuSn10–IN718 FGM part

IN718 and CuSn10 bimetallic structures were manufactured using a powder-based DED printer called AMBIT™ workstation (Hybrid Manufacturing Technologies, McKinney, TX). The powder material, injected through a coaxial nozzle interacts with laser heat power and forms a laser-induced molten pool. The presence of a heat transfer mechanism in the molten pool aids in the fabrication of near-net-shaped parts. Hybrid manufacturing refers to the combination of additive and subtractive processes in the same system. The additive component of the system is utilized to fabricate parts that later undergo post-processing using the subtractive component. DED attributes anisotropic material properties. As a result, DED-printed parts attain low surface quality sometimes higher dimensions than defined. Thus, subtractive machining will be aided to achieve dimensional accuracy per the designed geometry in the form of facing and contouring using the

CNC milling operation. The workstation uses a G-code input file derived from a computer-aided design (CAD) file containing the shape information. The input G-code file commands the machine process parameters while printing such as scanning speed, layer thickness, laser power, and powder feed rate. Nozzle gas prevents powders from melting onto the nozzle and clogging it. These alloys were printed onto a low-carbon steel substrate obtained from McMaster Cam.

Preliminary investigations were carried out to obtain the ideal process parameters for the chosen materials of CuSn10 and IN718. The most lucrative parameter set listed in Table 3 was selected to 3D print the intended bimetallic part. Each section has five layers, 0° and 90° rectilinear scanning strategy were implemented. The nominal thickness of each layer was defined as 0.54 mm, and a total of 10 layers were printed. To promote the flowability in the powder delivery hose and control the powder flight of CuSn10 particles from the powder cloud, a higher carrier gas flow rate and lower nozzle rate were selected.

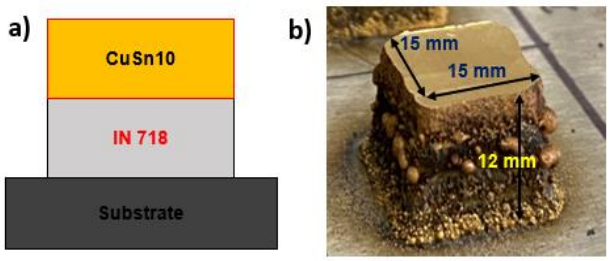

Fig. 3. DED fabricated IN718 – Cusn10 bimetallic part

In Laser-DED, the laser-induced plasma is intermittent due to heat flux undulations. Consequently, while anisotropic properties govern the structural characteristics of the as-deposited part which exasperate the dimensional accuracy [13], so the as-printed part attained higher layer thickness than the specified design. As shown in Fig. 3. a square block having dimensions 15 mm x 15 mm x 12 mm is fabricated using the AMBIT™ workstation. The schematic of the DED apparatus is depicted in Fig. 4. When creating the CuSn10 – IN718 FGM, the base part was first built with IN718, and then CuSn10 was stacked on top of it. A low-carbon steel substrate material is used as a build plate in this study.

Table 3. DED build parameters for IN718 and CuSn10

Variable	**Value**	
Powder type	**IN718**	CuSn10
# Layers	5	5
Power (W)	900	700
Scanning speed (mm/s)	10	10
Feed rate (g/min)	5	6
Carrier gas (L/min)	5	10
Nozzle gas (L/min)	9	8
Shield gas (L/min)	12	12

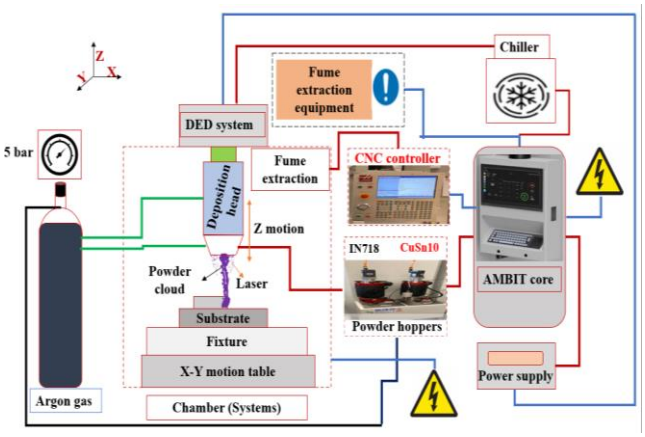

Fig. 4. Schematic diagram of DED-AM test bed

2.3. Metallographic preparation

The printed specimen was detached from the printed composite part using a wire-electric discharge machine (EDM). To ensure consistency in the results, all samples were produced from only one printed specimen. The chosen specimen, as shown in Fig. 5. was sectioned into 7 mm x 7 mm x 1 mm for each test procedure using the Buehler IsoMet High Speed Pro precision cutter. A grinder/polisher (Saphir 250 A1-ECO, Mager Scientific, United States) was used to prepare the samples for metallurgical analysis based on a four-step, as enlisted in Table 4 [14]. During grinding, the plate and sample holder rotates in a complementary (Comp.) direction whereas for polishing it is vice-versa (Contra.).

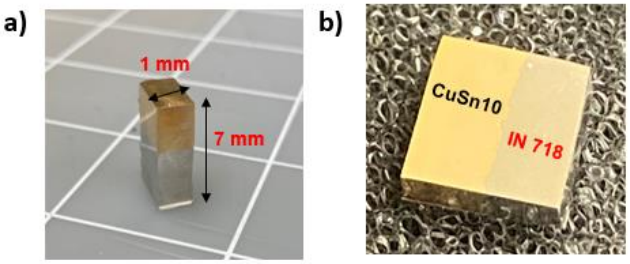

Fig. 5. Specimen for hardness EDS and Hardness testing

Table 4. Grinding and Polishing specifications

Surface	Abrasive/Size	Load (N)	Speed (rpm)/ Direction	Time (Min.)
CarbiMet Waterproof Disc	P500 to P 4000 grit SIC water cooled	25	240 - 300 Comp.	Until plane
TriDent cloth	9 µm diamond suspension	25	120 - 150 Contra	5
TriDent cloth	3 µm diamond suspension	25	120 - 150 Contra	4
Nanocloth	1 µm alumina suspension	25	120 - 150 Contra	3

2.3. Material testing

2.3.1. EDS analysis

Elemental identification and quantitative compositional information were conducted with a scanning electron microscope (SEM) equipped energy-dispersive x-ray spectroscope (EDS) (S4700, Hitachi, Japan). A silver paste was used to mount the sample to the holder. An accelerating voltage of 15kV and a beam current of 10μA were applied for both SEM and EDS analyses.

2.3.2. Micro-hardness measurement

Micro-hardness information across the sample surface is measured using a Vickers hardness tester (Model 900-390, Phase II+, United States). A load of 9.980N is applied for a duration of 15 seconds for each indentation. The indentations were performed along the build (Z) direction of the printed sample XZ plane to understand the hardness characteristics of the developed interface zone at IN718-CuSn10 bonding.

2.3.3. Thermoelectric property testing

Electrical conductivity and Seebeck coefficient changes analysis was carried out using a measuring device for thermoelectric (LSR-1100, Linseis, Germany) following the four-terminal method. The measurements were performed in the temperature range of approximately 313K to 383K. The environment was a low-pressure He environment. To derive elucidated understandings, three DED-AM printed samples were used, namely CuSn10, IN718, and IN718-CuSn10 in the electrical resistivity and Seebeck factor measurements, as shown in Fig. 6. The dimensions of the bimetallic part are 4 mm x 4 mm x 11 mm.

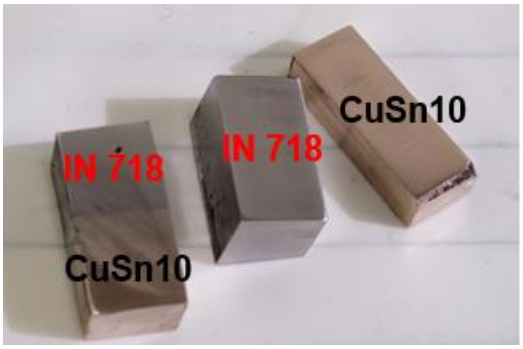

Fig. 6. Electrical resistivity and Seebeck coefficient test samples.

2.3.4. Compression test

A compressive strength test was conducted on a universal tester (AGS-X, Shimadzu, Japan) with a 10kN compressive load and a testing speed of 1.5mm/min to investigate the bonding behaviors at the interface of the FGM. A cylindrical specimen with a 5 mm [15] diameter and 22 mm length is chosen. Stress and stroke data were collected simultaneously.

3. Results and Discussions

3.1. Microstructural analysis

Microscopic images of the FGM displayed a defined interface with clear separation of the material regions between CuSn10 and IN718, indicating the presence of metallurgical bonding between the two materials, as shown in Fig 7. Though the interface of the FGM could be clearly distinguished, it is important to highlight that it did not appear to be a smooth separation. Additionally, CuSn10 particles were observed within the IN718 region and vice versa. As copper and nickel were aforementioned to be highly compatible with potential solubility, the previous findings were taxed on the effect of material diffusion between CuSn10 and IN718. The diffusion between the two materials created a complex interface which inherently resulted in varying properties at the interface of the FGM. Furthermore, due to the diffusion, there could be a secondary phase formation at the interface of the FGM. Further testing must nonetheless be conducted to identify such a secondary phase.

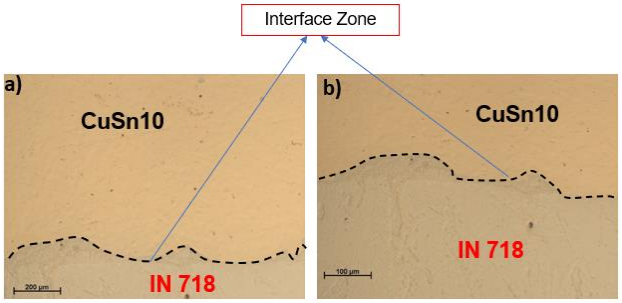

Fig. 7. Microscopic Images of the interface region at different resolution

In addition, common DED-printed defects were also displayed in the microscopic images. Pores, which resulted primarily from trapped air during the fabrication process, presented in both CuSn10 and IN718 regions, though those observed in the latter were larger in size. A surface crack as shown in SEM Fig. 8. caused by solidification shrinkage, might potentially intensify the material diffusion effect. The same defects were also reported by Karnati et al. [6] and Yadav et al. [16] in continuous Cu-Ni FGMs fabricated via preblended powder DED. Joining two dissimilar materials without compositional gradient has been previously discussed to be the cause of interfacial problems such as cracks or delamination [17].

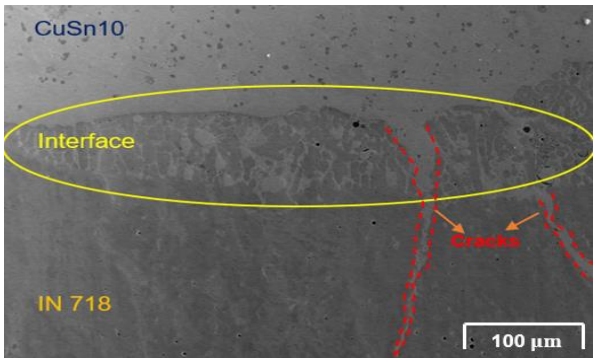

Fig. 8. SEM micrograph at FGM interface

The SEM and EDS analyses further validated the findings obtained from the microscopic imaging process. Here Fig. 8 is an SEM image that presents the defined regions of the FGMs, as well as the presented defects including porosity, cracks, and formed gradient zone or cross-region particle penetrations because of CuSn10 – IN718 direct bonding. Although no compositional altered layers were included in the current design and fabrication process; a gradient interface region was interpolated into the FGM via the effect of material diffusion. Studies [18-20] reported a combination of delamination and cracks at the interface zone due to the sharp transition of thermo-metallurgical properties. Despite that in this current study, as shown in Fig. 8 and Fig. 9 we only observed vertical cracks but not lateral cracks (delamination). The distinct thermal conductivities of CuSn10 and IN718 inherited thermal residual stresses and local strains at the gradient zone elude in form of cracks [21- 22]. Notably as displayed in Fig. 9, EDS scans detected enriched Mo, Nb, Fe, and Cr alloying elements diffused towards the CuSn10 region from IN718 due to surface tension and temperature gradient [23]. The reduction of mentioned elements in the IN718 matrix region promotes undesirable brittle intermetallic Laves phase that deteriorates its mechanical properties and genesis cracks as speculated in Fig. 8 [24-27]. In addition, the redistribution of elements insinuates to have formed a secondary phase with CuSn10.

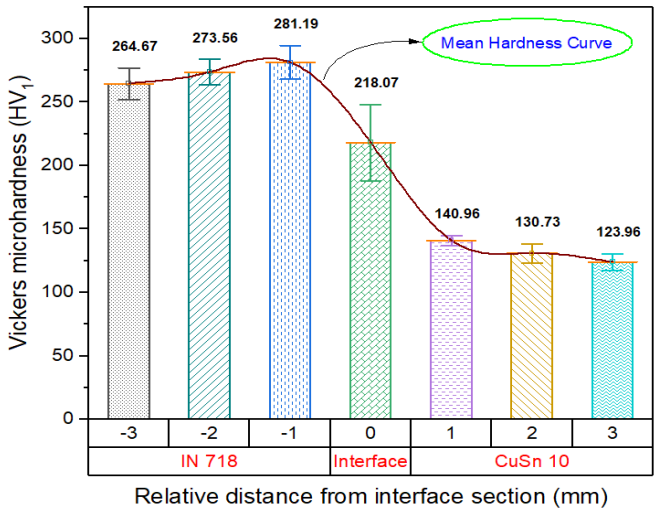

Fig. 10. Micro-hardness measurements of as-printed FGM CuSn10 – IN718 sample

Being softer and ductile material CuSn10 region displayed the lowest hardness across the specimen surface compared to the tougher IN718 region. These findings were consistent with the known characteristic of copper and nickel [28]. Most importantly, due to the dilution of CuSn10 into IN718, the hardness measured at the interface of the FGM reflected an improvement compared to the CuSn10 region.

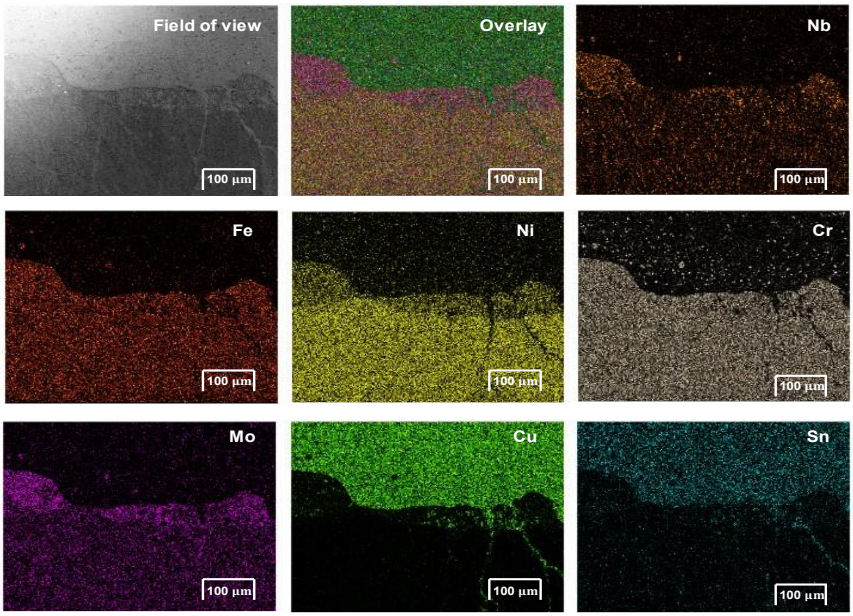

Fig. 9. EDS results at the FGM interface

3.2. Hardness distribution

The Vickers microhardness measurements are taken across the XZ surface of the CuSn10 – IN718 FGM along the build direction as shown in Fig. 10. A total of 7 hardness readings with 1000 µm spacing between indents was measured for every 1mm depth of the sample within a distance of 3 mm from the interface section of the two materials. Here "0 mm" depth indicates the interface section of the FGM sample.

As previously discussed, FGMs were expected to inherit the characteristics of their parent materials, allowing them to outperform single-material counterparts. In this case, the presence of IN718 enhanced the hardness at the interface section of the FGM. As reported in previous literature [16, 28], the sharp compositional gradation from one material to another in multi-metal bonding is the cause of such a steep reduction in hardness. The summary of hardness results for each zone is given in Table 5. Apparently, the gradation zone is highly influenced by elemental cross-transfer from origin

material zones, so it caused higher standard deviation as opposed to its counterparts. Furthermore, Fig. 10. demonstrated a significant decrease in hardness as departing from the interface towards both IN718 and CuSn10 regions, such difference evolves by virtue of heat accumulation on the previously deposited beneath layers. Thus, the hardness of either the IN718 or CuSn10 portion closer to the interface zone recorded higher values as compared to the portion that was farther away. Similarly, Zuback and Debroy [29] also attributed heat accretion leads to microstructural coarsening which facilitated diverse hardness results within the same material deposited builds.

Table 5. Microhardness test results

Zone	Mean (HV)	Standard Deviation (HV)	Min. (HV)	Max. (HV)
CuSn10	131.88	7.97	117.10	144.40
Interface	218.07	18.53	182.60	241.10
IN718	273.14	10.03	254.00	292.40

Here Min. and Max. stands for Minimum and Maximum

3.3. Electrical Conductivity and Seebeck coefficient

The analyses displayed evidence that electrical conductivity and the Seebeck coefficient changes were induced by the interface of the CuSn10 and IN718. Fig. 11 demonstrated the electrical resistivity of the three samples. Among the three samples, in the temperature range of 320 to 390K, CuSn10 displayed the lowest electrical resistivity, or in other words, the highest electrical conductivity, while IN718 the lowest. The electrical resistivity of the FGM specimen measured from the interface of the two materials was observed to be in the middle of this range. The finding further validating the previous discussion on the inheritance effect of FGM. While IN718 allowed for a higher hardness at the interface of the FGM, CuSn10 improves electrical conductivity.

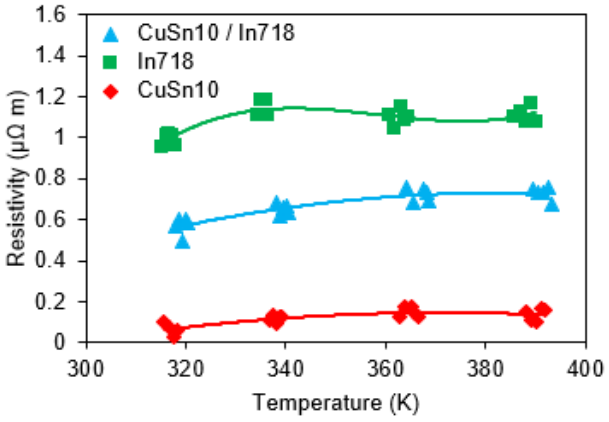

Fig. 11. Electrical resistivity of the CuSn10, IN718, and CuSn10 – IN718 samples

The results from the Seebeck coefficient change analysis are presented in Fig.12. The CuSn10 – IN718 FGM displayed the highest absolute Seebeck coefficient in the temperature range 320K to 390K. The change in the Seebeck coefficient of the FGM showed a 70% increase from the single material specimens. This boost indicated a reduction in carrier density across the interface, theorized to be influenced by the interface of the FGM.

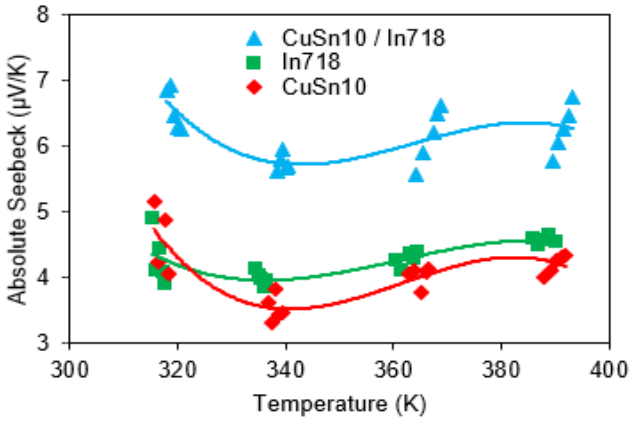

Fig. 12. Absolute Seebeck coefficient of the CuSn10, IN718, and CuSn10 – IN718 samples

3.4 Compression strength test

Here Fig. 13 illustrated the compressive stress-strain curve obtained for the CuSn10 – IN718 FGM part shown in Fig. 14a. The extracted yield strength, ultimate strength, elastic modulus, and elongation percentage were 170.7 MPa, 505.23 MPa, 8.8 GPa, and 17.45%. Indeed, compression test results drawn in this work are appositely matched with previous reports by Amit et. al [30] and Ahmed et. al. [31]. The key deformation namely 'folding deformation' is emerged mainly in the CuSn10 zone which precluded the acute deformation from reaching the interface. Except for the indulged effect of deformation in the CuSn10 region as shown in Fig. 14b, the rest of the specimen did not appear to be altered. Elemental diffusion constituted interfacial bond strength [24, 28] subsequently, there was no buckling nor deformation at or around the FGM interface which ensures the mechanical solidity of FGM structures.

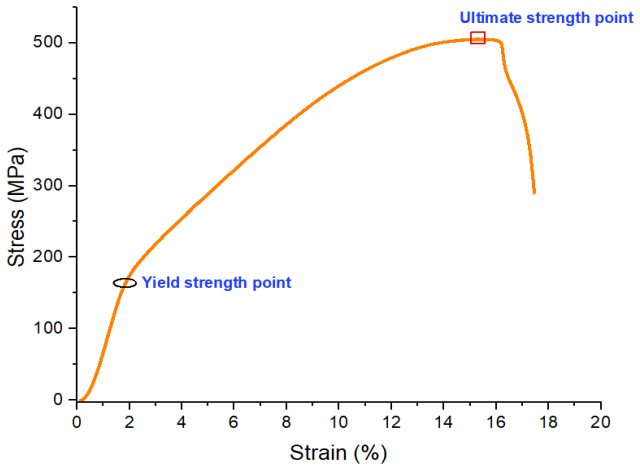

Fig. 13 Stress-strain curve of CuSn10 – IN718 sample

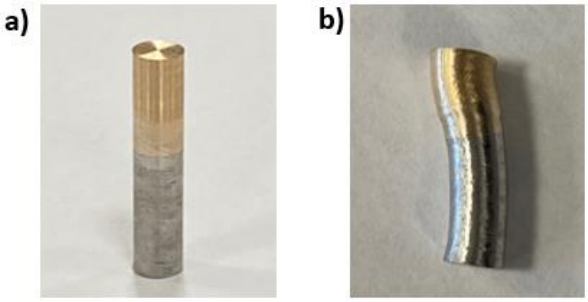

Fig. 14 Compressive strength test specimen a) before (left) and b) after (right)

4. Conclusion and Future work

The fabrication of CuSn10 – IN718 FGMs via laser-assisted powder-based DED using the AMBIT Hybrid system was successfully conducted and electrical resistivity, Seebeck coefficient, hardness, and compression properties are quantified, and interface zone properties are compared with pure metal regions.

- The specimens showcased evident metallurgical bonding at the interface between CuSn10 and IN718 was not smooth. Surface diffusion and penetration of one type of material into the other region were influenced by the high compatibility between copper and nickel, which created a complex and properties-variable interface.
- EDS mapping indicated redistribution of enriched Mo, Nb, Fe, and Cr elements might potentially cause a secondary phase with CuSn10.
- The hardness profile across the interface of the FGM exhibited an increase when departing from the CuSn10 region towards the interface and the IN718 region. The transition in hardness at the interface of the FGM is induced by the effect of IN718 elemental diffusion which proves the high compatibility of copper and nickel bonding.
- The electrical conductivity and Seebeck coefficient measurements further validated the inheritance effect of as-printed FGM. More importantly, the presence of CuSn10 significantly enhanced the electrical conductivity at the interface of the FGM in comparison to the IN718 sample.
- In addition, the absolute Seebeck coefficient of the FGM also reflected a 70% increase from the single-material region of the reduction in surface carrier density.
- The compression test findings attested neither deformation nor fracture being fostered at the FGM interface which ensured mechanical solidity of the CuSn10 – IN718 FGM part.

In the future, a constantan calibration sample will also be assessed to compare with the electrical performance of the printed samples. Also, thermal conductivity will be determined as similar to electrical conductivity tests. Additional microstructure analysis, such as transmission electron microscopy (TEM), will be conducted to investigate the secondary phase that existed in the interface region. Tensile strength properties will also be determined FGMs to understand their tensile behaviors.

Declaration of Competing Interest

The authors declare that they have no known competing for financial interests or personal relationships that could have appeared to influence the work reported in this literature.

Acknowledgment

The authors would like to extend the acknowledgments to the Foundation of the Statler College of Engineering and the Office of Vice President for Research at West Virginia University.

References

[1] Bhavar, V., Kattire, P., Thakare, S., Patil, S., & Singh, R. K. P. (2017). A Review on Functionally Gradient Materials (FGMs) and Their Applications. *IOP Conference Series*, *229*, 012021.

[2] Ghanavati, R., & Naffakh-Moosavy, H. (2021). Additive manufacturing of functionally graded metallic materials: A review of experimental and numerical studies. *Journal of Materials Research and Technology*, *13*, 1628–1664.

[3] Yan, L., Chen, Y., & Liou, F. W. (2020). Additive manufacturing of functionally graded metallic materials using laser metal deposition. *Additive Manufacturing*, *31*, 100901.

[4] Wang, Z., Wang, J., Xu, S., Liu, B., Sui, Q., Zhao, F., Gong, L. L., & Liu, J. (2022). Influence of powder characteristics on microstructure and mechanical properties of Inconel 718 superalloy manufactured by direct energy deposition. *Applied Surface Science*, *583*, 152545.

[5] de Almeida, D. S., Shimote, W. K., & Niwa, M. (1999). Selection of Materials for Combustion Chamber of Liquid Propellant Rocket Engine. In *XV Brazilian Congress of Mechanical Engineering, COBEM* (Vol. 99).

[6] Karnati, S., Sparks, T. E., Liou, F., Newkirk, J. W., Taminger, K. M. B., & Seufzer, W. J. (2015). Laser metal deposition of functionally gradient materials from elemental copper and nickel powders. In *2015 International Solid Freeform Fabrication Symposium*. University of Texas at Austin.

[7] Makarenko, K., Dubinin, O., & Shishkovsky, I. (2020). Analytical Evaluation of the Dendritic Structure Parameters and Crystallization Rate of Laser-Deposited Cu-Fe Functionally Graded Materials. *Materials*, *13*(24), 5665.

[8] Wang, Y., Liang, Z., Zhang, J., Ning, Z., & Guo, L. (2016). Microstructure and Antiwear Property of Laser Cladding Ni–Co Duplex Coating on Copper. *Materials*, *9*(8), 634.

[9] Rubio, W. M., Paulino, G. H., & Silva, E. C. N. (2012). Analysis, manufacture and characterization of Ni/Cu functionally graded structures. *Materials in Engineering*, *41*, 255–265.

[10] Yadav, S., Paul, C. P., Jinoop, A. N., Nayak, S. K., Rai, A. K., & Bindra, K. S. (2019, December). Effect of process parameters on laser directed energy deposition of copper. In *Gas Turbine India Conference* (Vol. 83532, p. V002T10A004). American Society of Mechanical Engineers.

[11] Hassanin, A. E., Scherillo, F., Prisco, U., Sansone, R., & Astarita, A. (2020). Selective laser melting of Cu-inconel 718 powder mixtures. *Journal of Manufacturing Processes*, *59*, 679–689.

[12] Pan, T., Zhang, X., Yamazaki, T., Sutton, A. T., Cui, W., Li, L., & Liou, F. W. (2020). Characteristics of Inconel 625—copper bimetallic structure fabricated by directed energy deposition. *The International Journal of Advanced*

Manufacturing Technology, *109*(5–6), 1261–1274.

[13] Fortes, F. J., Moros, J., Lucena, P., Cabalín, L., & Laserna, J. J. (2013). Laser-Induced Breakdown Spectroscopy. *Analytical Chemistry*, *85*(2), 640–669.

[14] Vander Voort, G. F. (2009). Metallographic specimen preparation for electron backscattered diffraction. *La Metallurgia Italiana*.

[15] Osipovich, K., Gurianov, D., Vorontsov, A., Knyazhev, E., Panfilov, A., Chumaevskii, A., ... & Kolubaev, E. (2022). Phase Formation, Microstructure, and Mechanical Properties of Ni-Cu Bimetallic Materials Produced by Electron Beam Additive Manufacturing. *Metals*, *12*(11), 1931.

[16] Yadav, S. R., Jinoop, A. N., Sinha, N., Paul, C. P., & Bindra, K. S. (2020). Parametric investigation and characterization of laser directed energy deposited copper-nickel graded layers. *The International Journal of Advanced Manufacturing Technology*, *108*(11–12), 3779–3791.

[17] Yang, S. H., Yoon, J., Lee, H., & Shim, D. (2022). Defect of functionally graded material of inconel 718 and STS 316L fabricated by directed energy deposition and its effect on mechanical properties. *Journal of Materials Research and Technology*, *17*, 478–497.

[18] Onuike, B., & Bandyopadhyay, A. (2018). Additive manufacturing of Inconel 718 – Ti6Al4V bimetallic structures. *Additive Manufacturing*, *22*, 844–851.

[19] Sridar, S., Klecka, M. A., & Xiong, W. (2022). Interfacial characteristics of P91 steel - Inconel 740H bimetallic structure fabricated using wire-arc additive manufacturing. *Journal of Materials Processing Technology*, *300*, 117396.

[20] Yuchao, B., Zhang, J., Zhao, C., Li, C., & Wang, H. (2020). Dual interfacial characterization and property in multi-material selective laser melting of 316L stainless steel and C52400 copper alloy. *Materials Characterization*, *167*, 110489.

[21] Chen, J., Yang, Y., Song, C., Zhang, M., Wu, S., & Wang, D. (2019). Interfacial microstructure and mechanical properties of 316L /CuSn10 multi-material bimetallic structure fabricated by selective laser melting. *Materials Science and Engineering A-Structural Materials Properties Microstructure and Processing*, *752*, 75–85.

[22] Carroll, B., Palmer, T. M., & Beese, A. M. (2015). Anisotropic tensile behavior of Ti–6Al–4V components fabricated with directed energy deposition additive manufacturing. *Acta Materialia*, *87*, 309–320.

[23] Mukherjee, T., Zuback, J., Zhang, W., & Debroy, T. (2018). Residual stresses and distortion in additively manufactured compositionally graded and dissimilar joints. *Computational Materials Science*, *143*, 325–337.

[24] Singh, G., Vasudev, H., Bansal, A., Vardhan, S., & Sharma, S. (2020a). Microwave cladding of Inconel-625 on mild steel substrate for corrosion protection. *Materials Research Express*, *7*(2), 026512.

[25] Kim, H., Grandhi, M., Liu, Z., Era, I. Z., & Zhang, H. (2022). Interface bonding behavior and failure mechanism of joining Tribaloy T-800/AISI 4140 via laser engineered net shaping. *Optics and Laser Technology*, *156*, 108620.

[26] Xiao, H., Li, S., Xiao, W., Li, Y., Cha, L., Mazumder, J., & Song, L. (2017). Effects of laser modes on Nb segregation and Laves phase formation during laser additive manufacturing of nickel-based superalloy. *Materials Letters*, *188*, 260–262.

[27] Xie, H., Yang, K., Li, F., Sun, C., & Yu, Z. (2020). Investigation on the Laves phase formation during laser cladding of IN718 alloy by CA-FE. *Journal of Manufacturing Processes*, *52*, 132–144.

[28] Onuike, B., Heer, B., & Bandyopadhyay, A. (2018a). Additive manufacturing of Inconel 718—Copper alloy bimetallic structure using laser engineered net shaping (LENS^{TM}). *Additive Manufacturing*, *21*, 133–140.

[29] Zuback, J., & Debroy, T. (2018). The Hardness of Additively Manufactured Alloys. *Materials*, *11*(11), 2070.

[30] Onuike, B., & Bandyopadhyay, A. (2019). Bond strength measurement for additively manufactured Inconel 718-GRCop84 copper alloy bimetallic joints. *Additive Manufacturing*, *27*, 576–585.

[31] Nassef, A. M., & El-Hadek, M. A. (2016). Microstructure and Mechanical Behavior of Hot Pressed Cu-Sn Powder Alloys. *Advances in Materials Science and Engineering*, *2016*, 1–10.

Declaration of interests

☒The authors declare that they have no known competing financial interests or personal relationships that could have appeared to influence the work reported in this paper.

☐The authors declare the following financial interests/personal relationships which may be considered as potential competing interests: